


FULL PAPER

Open Access



Reappraisal of volcanic seismicity at the Kirishima volcano using machine learning

Yohei Yukutake^{1*} , Ahyi Kim² and Takao Ohminato¹

Abstract

Volcanic earthquakes provide essential information for evaluating volcanic activity. Because volcanic earthquakes are often characterized by swarm-like features, conventional methods using manual picking require considerable time to construct seismic catalogs. In this study, using a machine learning framework and a trained model from a volcanic earthquake catalog, we obtained a detailed picture of volcanic earthquakes during the past 12 years at the Kirishima volcano, southwestern Japan. We detected ~6.2 times as many earthquakes as a conventional seismic catalog and obtained a high-resolution hypocenter distribution through waveform correlation analysis. Earthquake clusters were estimated below the craters, where magmatic or phreatic eruptions occurred in recent years. Increases in seismic activities, *b* values, and the number low-frequency earthquakes were detected before the eruptions. The process can be conducted in real time, and monitoring volcanic earthquakes through machine learning methods contributes to understanding the changes in volcanic activity and improving eruption predictions.

Keywords Volcanic earthquake, Machine learning, Phase picking, Kirishima volcano

*Correspondence:

Yohei Yukutake

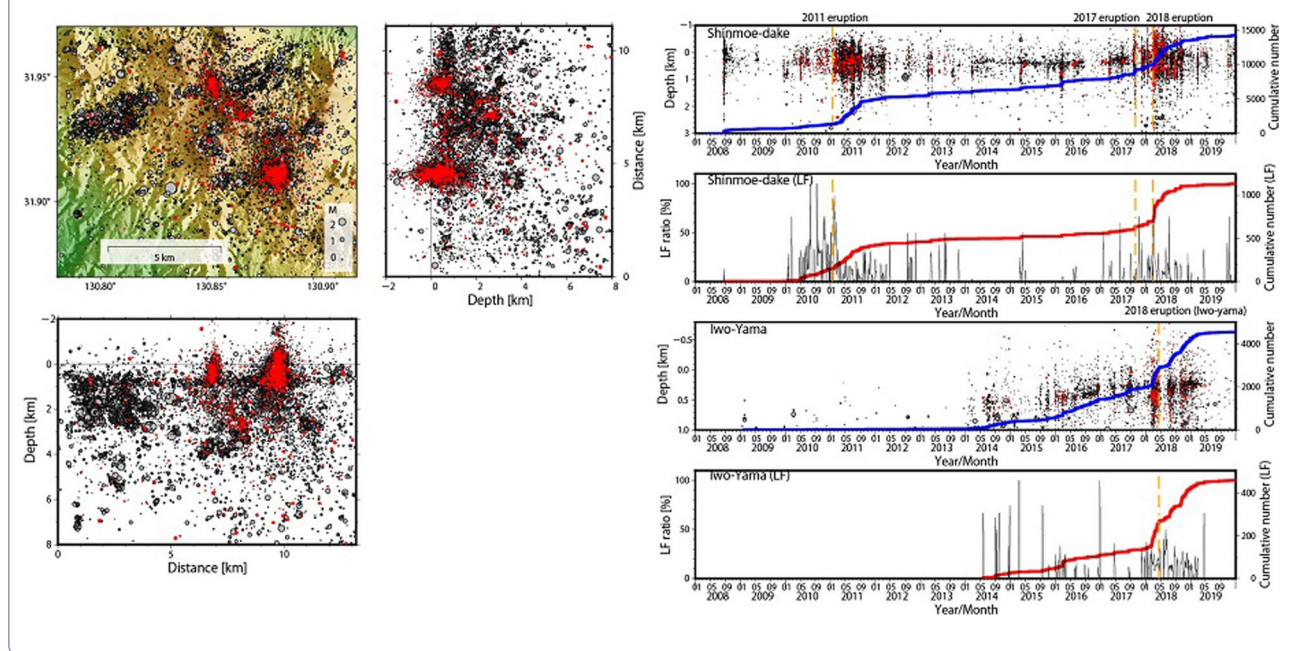
yukutake@eri.u-tokyo.ac.jp

Full list of author information is available at the end of the article



© The Author(s) 2023. **Open Access** This article is licensed under a Creative Commons Attribution 4.0 International License, which permits use, sharing, adaptation, distribution and reproduction in any medium or format, as long as you give appropriate credit to the original author(s) and the source, provide a link to the Creative Commons licence, and indicate if changes were made. The images or other third party material in this article are included in the article's Creative Commons licence, unless indicated otherwise in a credit line to the material. If material is not included in the article's Creative Commons licence and your intended use is not permitted by statutory regulation or exceeds the permitted use, you will need to obtain permission directly from the copyright holder. To view a copy of this licence, visit <http://creativecommons.org/licenses/by/4.0/>.

Graphical Abstract



Introduction

Volcanic earthquakes, including volcano-tectonic and low-frequency earthquakes, are activated in response to the migration of magma or hydrothermal fluids (Hayashi and Morita 2003; Kato et al. 2015; Shelly et al. 2013) or changes in the stress field (Toda et al. 2002). They provide important information for evaluating volcanic activities (e. g., McNutt 1996). To accurately evaluate the characteristics of earthquake activity, a precise seismic catalog must be constructed. The construction of an accurate seismic catalog on a real-time basis is also desirable for improving eruption forecasting and hazard assessment. In conventional procedures for constructing an earthquake catalog, an earthquake is detected using an indicator, such as the ratio of the short-time average to the long-time average of waveform amplitude (STA/LTA). Then, the arrival time and amplitude of the seismic phase are picked through visual inspection to obtain reliable hypocenter locations and magnitudes. Consequently, obtaining a precise seismic catalog is time-consuming.

In volcanic or geothermal regions, earthquake swarms are often observed during the activation of volcanic activity, where numerous volcanic earthquakes occur during a short period. As seismic waves from many events crowd into the waveform record with a short-time range, detecting earthquakes and picking seismic phases are more complicated, even for expert researchers and seismic analysts. In this regard, the matched filter method (e.g., Peng

and Zhao 2009; Shelly et al. 2007) is a powerful tool for detecting earthquakes in crowded waveform records. However, this method involves cross-correlation analysis using the waveforms of template earthquakes and continuous waveforms. Therefore, detection is difficult when an earthquake occurs in a location different from the template earthquakes or when the waveform characteristics temporally change because of changes in focal mechanisms or the surrounding medium, even in identical locations. In addition, as the number of template earthquakes increases, the computational cost increases and real-time processing becomes more difficult.

Recently, automatic event detection and phase picking using machine learning (ML) have been developed (e. g., Mousavi et al. 2020; Ross et al. 2020; Zhu and Beroza 2019). These methods reveal detailed seismicity images that cannot be obtained using conventional methods. For example, Ross et al. (2020) detected crustal earthquakes in Southern California and revealed highly resolved fault structures from the hypocenter distribution and temporal changes in the hypocentral area related to the migration of crustal fluid within fault zones. Meanwhile, Wilding et al. (2022) revealed the detailed structure of a sill complex in the deep part of the Hawai'i volcanic system using a high-resolution earthquake catalog with a ML procedure. In addition to phase picking, based on ML, reliable information on seismic activity can be estimated using clustering based on waveform similarity

(Perol et al. 2018), the spatial pattern of wave propagation (Sugiyama et al. 2021), arrival time differences from station-pair cross-correlation (Gal et al. 2021; Poiata et al. 2016), and classification of the seismic event type (Nakano et al. 2019).

Although the application of ML in monitoring seismic activity has been widely promoted, its application in volcanic regions remains challenging. One reason is that the existing trained models are created from the seismic catalog of ordinary (tectonic) earthquakes and may not fully reflect the characteristics of volcanic earthquakes. It has been reported that applying optimally trained models matched to a target region improves the detection and phase picking performance (Münchmeyer et al. 2022). Kim et al. (2023) constructed a deep learning model to detect seismic phase onset using a precise catalog of volcanic earthquakes at the Hakone volcano in central Japan. They showed that the model improved the detection rate and accuracy of phase picking for volcanic earthquakes compared with the original trained model developed by Zhu and Beroza (2019), which they used as the starting model. Furthermore, volcanic regions often lack precise seismic catalogs based on manual picking data. Therefore, for such a region, it is difficult to construct a trained model using the seismic events that occurred there. One of the objectives of this study is to evaluate the applicability of trained models developed based on seismic catalogs for a given volcano to estimate seismic activity in other volcanic regions. We applied the architecture of ML developed by Zhu and Beroza (2019) and the trained model by Kim et al. (2023) to seismic data from the Kirishima volcano and discussed its applicability for monitoring volcanic earthquakes.

The Kirishima volcanic complex is located in southern Kyushu, Japan, and comprises more than 20 stratocones and maars (Fig. 1a). During the last 1000 years, magmatic activity, including the eruption of basaltic and andesitic lava flows and tephra, has occurred mainly at the Shinmoedake, Ohachi, and Iwo-Yama volcanoes (Imura and Kobayashi 2001). In 1716–1717, an explosive magmatic eruption occurred at Shinmoedake. An eruptive volume of 0.2 km^3 was estimated for this eruption (Imura and Kobayashi 1991). Smaller eruptions occurred in 1822, 1959, and 1991 at Shinmoedake. Since 2008, volcanic activity at Shinmoedake has gradually increased. Small

phreatic eruptions occurred in August 2008 and March–July 2010. The first large-scale magmatic eruption in ~ 300 years occurred in January 2011 as a sub-Plinian eruption. During this eruption, $\sim 0.03 \text{ km}^3$ of magma erupted (e.g., Nakada et al. 2013). Phreatomagmatic eruptions occurred again in October 2017, followed by a magmatic eruption in May 2018, during which $\sim 10^8 \text{ kg}$ of tephra and $1.5 \times 10^7 \text{ m}^3$ of lava erupted (e.g., Maeno et al. 2023). Around Iwo-Yama, located $\sim 5\text{-km}$ northwest of Shinmoedake, a fumarole has been active since December 2015, and a phreatic eruption occurred in April 2018 (e.g., Tajima et al. 2020).

Several studies have reported the activity of volcanic earthquakes at the Kirishima volcano based on a seismic catalog obtained using a conventional event detection method (Fukuoka District Meteorological Observatory and Kagoshima Local Meteorological Observatory 2013; Yamada et al., 2019). However, the detailed spatial–temporal distribution of volcanic earthquakes and their relation to eruptive activities have not been fully clarified. Thus, another purpose of this study is to provide a detailed estimate of the volcanic seismic activity at the Kirishima volcano. We estimated a highly resolved hypocenter distribution based on phase picking data using the ML method to obtain further information associated with volcanic activity. We also estimated the temporal change in b values and event types using the frequency index.

Data and methods

Seismic observation

We used continuous waveform data from the past 12 years (2008–2019) recorded at 30 permanent stations installed in and around the Kirishima volcano (Fig. 1a) by the Earthquake Research Institute of the University of Tokyo (ERI), the Japan Meteorological Agency (JMA), the National Research Institute for Earth Science and Disaster Resilience (NIED), and Kyushu University (Fig. 1a). The average station spacing at the Kirishima volcano is $\sim 2 \text{ km}$. Broadband seismometers are installed at ERI stations, whereas short-period seismometers with a natural period of 1 Hz are installed at other stations. Seismic waveforms were continuously recorded at 100-Hz sampling intervals at all stations.

(See figure on next page.)

Fig. 1 Map and seismicity at the Kirishima volcano. **a** Map of the Kirishima volcano showing the locations of permanent seismic stations. The inset shows the target regions with respect to the western part of the Japanese island. The orange rectangle corresponds to that shown in **(b)**. **b** Hypocenter distribution of earthquakes beneath the Kirishima volcano for the hypocenter catalog based on ML. The top panel shows the epicentral distribution, and the right and bottom panels indicate the depth distribution along the N–S and E–W sections, respectively. The depth of 0 km corresponds to the sea level. The red circles indicate the locations of low-frequency earthquakes classified based on the frequency index (FI)

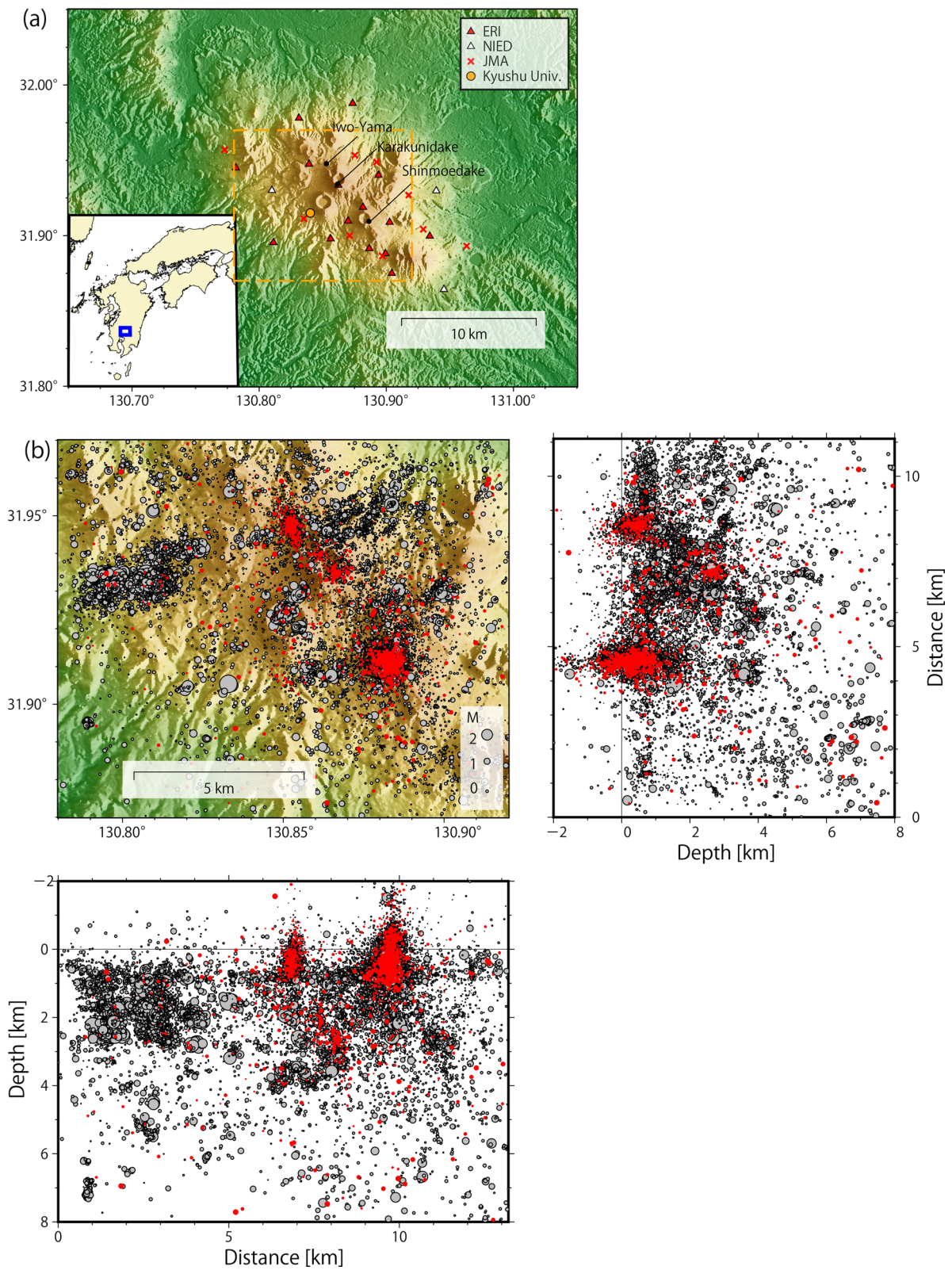


Fig. 1 (See legend on previous page.)

Phase picking and hypocenter determination

We conducted the following processing for every hour of continuous waveform recording. The continuous waveform recordings were preprocessed by removing the offset and trend and then applying a 1-Hz high-pass filter to reduce the contamination of low-frequency noise. For each station, phase picking was performed using the PhaseNet architecture developed by Zhu and Beroza (2019) with a trained model developed by Kim et al. (2023). This model was created based on a seismic catalog of ~30,000 volcanic earthquakes at Hakone volcano over the past 20 years, while the original model by Zhu and Beroza (2019) was trained using manually picked seismic traces from tectonic earthquakes in northern California. The volcanic earthquake activity in the Hakone and Kirishima regions is similar, as both exhibit several earthquakes with small epicentral distances and a large fraction of volcano-tectonic earthquakes with clear *P*- and *S*-wave onsets. In contrast, low-frequency earthquakes have less distinguishable onsets and display a lower frequency component than volcano-tectonic earthquakes of comparable magnitude. In addition, the instrumentation installed at Hakone volcano mainly comprises short-period seismographs, while broadband seismographs are mainly used at the Kirishima volcano.

To create their trained model, Kim et al. (2023) used 217,5553 seismic waveforms, each containing one manually picked *P*- and *S*-wave onset readings. Based on these data, they created two trained models: (1) a model trained from scratch using the PhaseNet architecture (Model 1) and (2) a fine-tuned model derived from the original PhaseNet-trained model (Model 2). The Model 1 results improved the F1 score (e.g., Zhu and Beroza 2019) for *P*- and *S*-wave arrival times using validation data based on the seismic waveforms at Hakone volcano beyond that obtained with Model 2 and the original trained model by Zhu and Beroza (2019). The F1 scores for the *P*-wave arrivals in the original PhaseNet model, Model 1, and Model 2 are 0.823, 0.860, and 0.857, respectively, and those for the *S*-wave arrivals are 0.641, 0.755, and 0.749. Furthermore, Kim et al. (2023) demonstrated improved probabilities for *P*- and *S*-wave onsets in the waveform records including events with multiple distinct amplitudes by using the trained model.

In this study, we chose Model 1 by Kim et al. (2023) to use as a trained model and selected a value of 0.3 as the threshold for the normalized probability density functions for identifying *P*- and *S*-wave onsets. Phase association was conducted on the *P*- and *S*-wave arrival times picked by PhaseNet using the REAL code developed by Zhang et al. (2019). We set thresholds of ≥ 3 stations and ≥ 2 stations for *P*- and *S*-waves, respectively, to identify the same event. For the phase association, the

theoretical arrival time from an assumed source to each station was calculated using the 1-D velocity structure beneath the Kirishima volcano that has been used for routine hypocenter determination at the ERI Kirishima Volcano Observatory (Mikada 1996). Seismic phases attributed to the same event by the REAL code were then used to determine hypocenter locations following the method of Hirata and Matsu'ura (1987). Their approach combines a maximum-likelihood method with a 1-D velocity model to obtain the hypocenter location via the inversion of absolute arrival times. The local magnitude was determined based on the maximum amplitude following the empirical relation established by Watanabe (1971). The hypocenter locations of 61,402 earthquakes were estimated over a period of 12 years.

We improved the original 1-D velocity structure (Mikada 1996) and estimated station corrections using the JHD method (Kissling et al. 1994) to obtain reliable absolute earthquake locations. In this analysis, we used earthquakes with at least eight phase pickings of both *P*- and *S*-waves obtained using the above procedure. We excluded events whose picking data showed travel time residuals ≥ 1.5 s for the initial hypocenter determinations. As a result, we used 4000 events to estimate the 1-D velocity model and station corrections. Given the estimated 1-D velocity structure and station corrections (Additional file 1: Fig. S1), the hypomh_ps code (Kawaniishi et al. 2009) was used to determine the hypocenter only for each earthquake with at least four phase pickings of *P*- and *S*-waves. The hypomh_ps code is a modified version of Hirata and Matsu'ura (1987) that allows the application of 1-D velocity structures to *P*- and *S*-waves separately. We obtained the initial hypocenters of 57,357 events. By applying the modified 1-D velocity mode and station corrections, the travel time residuals for the *P*- and *S*-waves were improved (Additional file 1: Fig. S2). The root-mean-square residuals of travel time decreased from 0.151 to 0.112 s for *P*-waves and from 0.290 to 0.226 s for *S*-waves.

We relocated the hypocenters using the double difference (DD) method (Waldhauser and Ellsworth 2000). In addition to the relative arrival time data (catalog data) obtained by PhaseNet, we also used relative travel time data through waveform correlation analysis (cross-correlation data). Waveforms within a time window of 0.1 s before and 0.4 s after the *P*- or *S*-wave arrival times were used for correlation processing. For stations, where picking data were not available, the waveforms were trimmed based on the theoretical arrival time using a time window of the same length. We used cross-correlation data with a cross-correlation coefficient ≥ 0.8 . Consequently, 4.6 million station pairs for catalog data and 12.5 million station pairs for cross-correlation data were applied to the DD

method. To conduct relocation using the DD method, earthquakes with large travel time residuals (defined as values greater than or equal to 6 times the standard deviation of the travel time residuals) or with a determined depth above ground level were eliminated. After applying the DD method, the locations of 41,349 events were finally obtained; we call this hypocenter catalog the ML catalog. The JMA catalog contains 6401 events within the same period.

***b* Values**

We estimated the temporal variation of *b* values for the earthquakes beneath Shinmoedake and Iwo-Yama using the ZMAP code (Wiemer 2001). The *b* value is defined by the following equation:

$$\log N = a - bM \quad (1)$$

Earthquakes were selected using a time window that stretched and contracted to include a constant number of events, chosen as 300. We estimated the *b* and *a* values in Eq. (1) using the maximum-likelihood estimate method (Aki 1965) for earthquakes that met the criteria $M \geq M_c$, where M_c is the completeness magnitude. For reliable estimation of *b* values, we estimated the *b* value only for data sets within the time window for which the number of events with $M \geq M_c$ was above 200 (Roberts et al. 2015). The confidence regions for the *b* and *a* values were estimated by 100-bootstrap resampling. Following the workflow proposed by Roberts et al. (2015) to validate the optimal estimation for M_c , we estimated the temporal variation in the *b* value using three methods: the maximum curvature (Wiemer and Wyss 2000) (Additional file 1: Fig. S3), goodness of fit (GFT) (Wiemer and Wyss 2002) (Additional file 1: Fig. S4), and *b* value stability (BVS) (Cao and Gao 2002) methods (Additional file 1: Fig. S5). According to Roberts et al. (2015), it is recommended to use the BVS method, if M_c can be stably estimated. However, for our seismic catalog, M_c estimation via the BVS method was unstable, yielding a large *b* value error. In contrast, the *b* value error as computed using the GFT method was small (< 0.25 for most time windows for earthquakes beneath Shinmoedake). Following the workflow of Roberts et al. (2015), we considered the *b* value result obtained using the GFT method acceptable. Following the results of Gulia et al. (2016), the time window was shifted by one event. We also estimated the magnitude bandwidth (e.g., Konstantinou 2022), which is defined as the difference between the maximum magnitude and M_c in each time window. The seismic catalog was split before and after the occurrence time of the eruptions to avoid mixing pre-seismicity and post-seismicity data for the eruption. In the GFT method, we estimated the synthetic magnitude–frequency distribution

using the optimal *b* and *a* values for each minimum magnitude to evaluate the GFT of the power law based on the following equation:

$$R(a, b, M_i) = \frac{\sum_{M_i}^{M_{\max}} |B_i - S_i|}{\sum_i B_i} \times 100, \quad (2)$$

where B_i and S_i are the observed and synthetic cumulative number of events in each magnitude bin, respectively, M_i is the minimum magnitude, and *R* is the residual defined as the GFT for the power law distribution. In this study, we defined M_i that minimized the residual as M_c . We considered *b* values with residuals $\leq 10\%$ as a reliable estimation.

Frequency index

We classified the type of seismic signal based on the frequency index (FI) (Helena and Michael 2010; Matoza et al. 2014) as defined by the following equation:

$$FI = \log_{10} \left(\frac{A_H}{A_L} \right) \quad (3)$$

where A_H and A_L represent the average spectral amplitude within the high-frequency and low-frequency bands, respectively. The types of volcanic earthquakes are labeled in the JMA catalog (Additional file 1: Figs. S6, S7 and S8). Examples of spectra for volcano-tectonic and low-frequency earthquakes (defined by A- and B-type earthquakes, respectively, following the definition of Minakami (1974)) are shown in Additional file 1: Fig. S9. Low-frequency earthquakes had significant amplitude in the frequency range of 1–4 Hz compared with those of volcano-tectonic earthquakes. Therefore, to classify these events, we defined the ratio of the average amplitude over the 1–4 Hz range to the average amplitude over the 10–15 Hz range as FI. We used the waveform record at the stations within 5 km from the epicenter to reduce the path effect. For the horizontal components at each station, the spectra were calculated using a time window of 4 s from the theoretical arrival time of the *S*-wave. The noise waveform was obtained using a time window of 2 s from 3 s before the theoretical arrival time of the *P*-wave, and the spectrum for the noise waveform was obtained. The signal-to-noise (SN) ratio was defined as the ratio of the average amplitude of spectra for the signal and noise waveforms within the 1–4 Hz and 10–15 Hz ranges. FI was calculated only for events with ≥ 3 stations having an SN ratio greater than 2 within both frequency ranges. We found that the frequency distribution of the FI values at a given station displays an offset over the entire distribution (Additional file 1: Fig. S10a, b). Following the method given by Wilding et al. (2022), we applied a station correction to each station by subtracting the median of all

FI values at that station from the estimated FI values. After applying the station correction, we averaged the FI values for all stations and components and assigned it as the final value for each event. We could estimate the FI values for 38,761 events. The frequency distribution of the standard deviation of the FI values, estimated from the FI values at the available stations, is shown in Additional file 1: Fig. S10c. Most standard deviations are less than 0.2.

The relationships between FI and magnitude for the JMA and ML catalogs are shown in Additional file 1: Fig. S11a, b, respectively. Most of the earthquakes identified as low-frequency earthquakes in the JMA catalog have $FI < -0.2$. In addition, there were no low-frequency earthquakes with $M > 0.6$ in the JMA catalog. In the ML catalog (Additional file 1: Fig. S11b), another trend is observed between the FI values and magnitudes in the range $FI < -0.2$ and magnitude ≤ 0.6 . Based on the results from the JMA catalog (Additional file 1: Fig. S11a) and the standard deviation of the final FI values (Additional file 1: Fig. S10c), we categorized events that fell within the range $FI < -0.4$ and magnitude ≤ 0.6 as low-frequency earthquakes. Examples of waveforms classified as low-frequency and volcano-tectonic earthquakes in the ML catalog based on the FI value are shown in Additional file 1: Fig. S11c, d, respectively.

Results

The hypocenter distribution of the ML catalog is shown in Fig. 1b. For comparison, we also show the hypocenter distribution based on the JMA catalog in Additional file 1: Fig. S6. We also show the time–depth distribution and cumulative number of earthquakes beneath the Kirishima volcano in Fig. 2. The magnitude–frequency distributions of the ML and JMA catalogs are shown in Additional file 1: Fig. S8. We obtained ~ 6.2 times as many earthquakes as the JMA catalog using ML. The magnitude completeness was -0.8 for the ML catalog, whereas that of the JMA catalog was 0.0, indicating an improvement in the detectability of earthquakes. Clusters of volcanic earthquakes were identified beneath Shinmoedake, Iwo-Yama, and in the western part of the Kirishima volcano in both catalogs (Figs. 1b, 3, and Additional file 1: Fig. S6). However, the ML catalog revealed a detailed

pattern of seismic activities associated with eruptive activities beneath Shinmoedake and Iwo-Yama.

The seismic activity beneath Shinmoedake is shown in Figs. 2c, d, and 3a. Beneath Shinmoedake, numerous small volcanic earthquakes occurred in the depth range from -0.5 to 3 km below the crater (Depth of 0 km corresponds to sea level), showing a vertical hypocenter lineament that may reflect the magma pathway. At Shinmoedake, several eruptive events occurred: small phreatic eruptions in August 2008 and March–July 2010, a sub-Plinian eruption on January 26, 2011, phreatomagmatic eruption on October 11, 2017, and a magmatic eruption on March 1, 2018. Although the corresponding earthquake cluster is also identified in the JMA catalog (Additional file 1: Fig. S6), our proposed method revealed the detailed time sequence of seismic activity. The seismic activity was gradually activated toward the 2011 magmatic eruption since 2010. The activity in the shallow part of the crater was also enhanced from March 2017, preceding the 2017 eruption. The upper depth of the seismicity area became shallower toward the 2017 eruption since March 2017 (Fig. 2c). After the 2017 eruption, the seismic activity was quiescent for ~ 1 month. From December 2017, the earthquakes were activated again, showing a burst-like increment, leading to the 2018 eruption. The seismic activity remained high after the 2018 eruption until October 2018.

The seismic activity beneath Iwo-Yama is shown in Figs. 2e, f, and 3b. Volcanic earthquakes are concentrated in the depth of -0.5 to 0.5 km below sea level beneath Iwo-Yama. A phreatic eruption occurred on April 19, 2018, at Iwo-Yama. In this area, seismic activity has increased since 2014. The upper depth limit of seismicity became shallower toward the 2018 eruption (Fig. 2e). Moreover, before the eruption, seismic activity was remarkably activated since the end of February 2018. Seismic activity quiesced for a month after the eruption and was activated again from late June 2018 through April 2019.

Low-frequency earthquakes were concentrated in an area just beneath the Shinmoedake and Iwo-Yama craters. Another cluster of low-frequency earthquakes was also identified at a depth of 3 km below Karakuni-dake (Fig. 1b). The temporal seismicity pattern indicates a

(See figure on next page.)

Fig. 2 Depth–time distribution and cumulative number of earthquakes. The red circles correspond to low-frequency (LF) earthquakes. The blue and red lines show the cumulative curves of the volcanic and LF earthquakes, respectively. The dotted vertical yellow lines show the occurrence times of main events: the 2011 Shinmoedake eruption, the 2016 Kumamoto earthquake, the 2017 and 2018 Shinmoedake eruptions, and the 2018 Iwo-Yama phreatic eruption. **a** Whole region, **c** Shinmoedake, and **e** Iwo-Yama. Panels **b**, **d**, and **f** show the cumulative curve of LF earthquakes and the ratio of LF earthquakes to volcano-tectonic earthquakes (thin black line) in each region. We used a time window of 7 days, moving at 2-day intervals, to estimate the LF ratio. The Shinmoedake and Iwo-Yama regions correspond to the maps shown in Fig. 3a, b, respectively

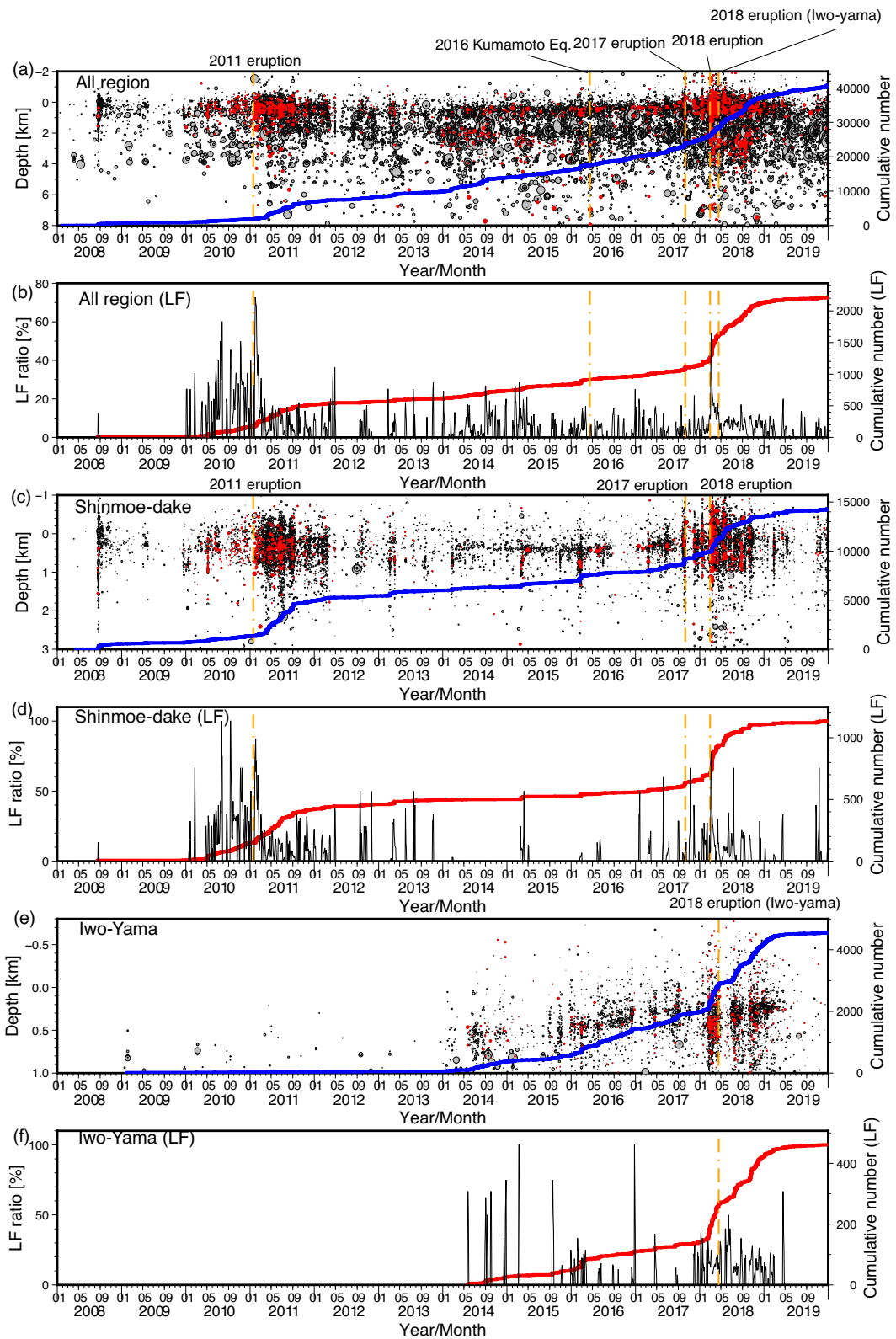
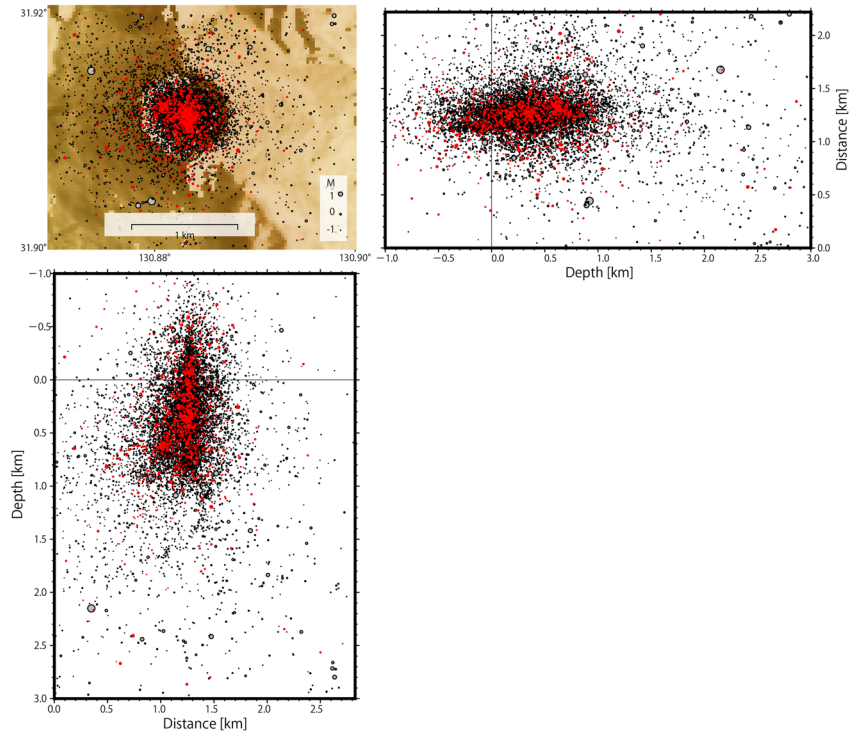


Fig. 2 (See legend on previous page.)

(a) Shinmoe-dake



(b) Iwo-Yama

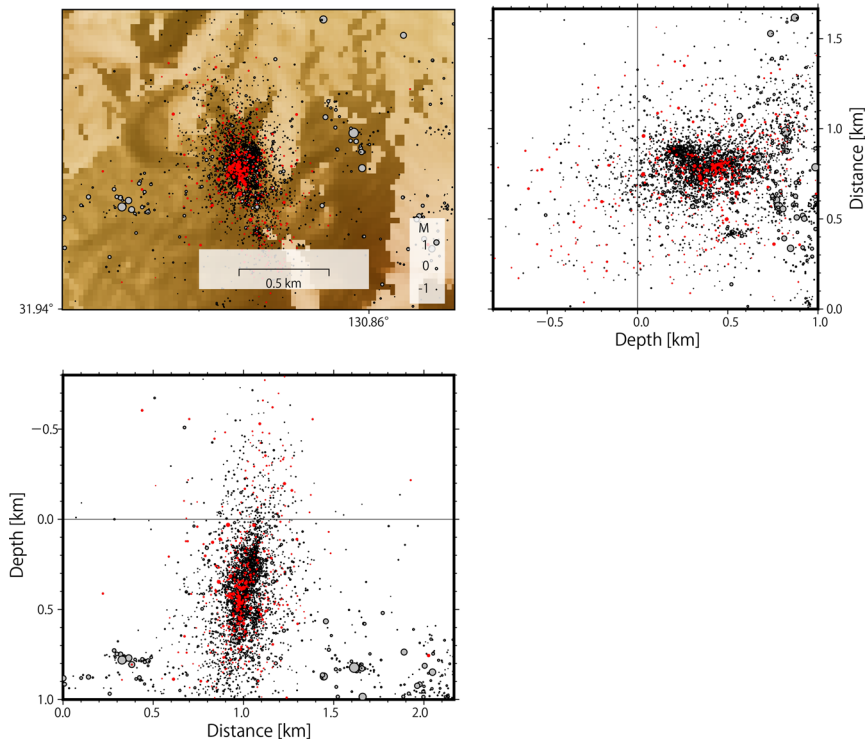


Fig. 3 Hypocenter distributions beneath Shinmoedake and Iwo-Yama. **a** Hypocenter distribution of earthquakes beneath Shinmoedake. (top) Epicentral distribution and (right and bottom) depth distributions along the N–S and E–W sections. Red circles correspond to the hypocenters of low-frequency earthquakes. **b** Hypocenter distribution of earthquakes beneath Iwo-Yama

greater number of low-frequency earthquakes just below Shinmoedake and Iwo-Yama prior to the eruptions (Fig. 2d, f). A slight additional increase in the number of low-frequency earthquakes was also observed from 2014 to 2015 (Fig. 2b).

The temporal changes in b values within the two regions are shown in Fig. 4. The b values of earthquakes beneath Shinmoedake (Fig. 4a) exceeded 1.1 before the 2011 eruption. After the 2011 eruption, the b values remained high, dropped temporarily, and again increased at the end of 2011. The b value rose again to a high value of 1.5 in early 2013 and then gradually declined through 2015, showing slight fluctuations. From the beginning of 2017, it increased again toward the 2017 eruption. After the eruption, the b values increased again toward the 2018 magmatic eruption. Although the fitness for the Gutenberg–Richter law is not very good in the Iwo-Yama region (Fig. 4b), the b value increased through the middle of 2015, decreased at the end of 2016, and then increased again in 2017. After one drop, we see an abrupt increase in the b values just before the 2018 phreatic eruption at Iwo-Yama.

Discussion and conclusions

In this study, we developed a seismic catalog for the Kirishima volcano using automatic phase picking based on the ML framework. The resulting catalog was improved in terms of detectability compared with the JMA catalog based on manual phase picking (Additional file 1: Fig. S8). Even using the trained model derived from the hypocenter catalog at a different volcano, we obtained a detailed history of volcanic earthquakes at the Kirishima volcano, which supports the idea that the trained model can be applied to other volcanic regions. Following the 2016 Kumamoto earthquake in the central part of Kyushu, when numerous aftershocks occurred (e.g., Asano and Iwata 2016), the seismicity beneath the Kirishima volcano did not change according to both manual and automatic seismic catalogs (Fig. 2a, Additional file 1: Fig. S7). This result implies that even when the waveforms recorded in the study area were contaminated by wave trains from outside the study area, event detection based on ML caused hardly any false detection.

Kim et al. (2023) demonstrated that the detectability of events using Model 1 is often low when multiple events are contained within a single waveform trace. To improve detection performance in such cases, they created two additional trained models using 100,000 semisynthetic training data, each containing two randomly selected events within each waveform trace. The first model was trained from scratch using the original PhaseNet-trained model (Model 3), and the second was a fine-tuned version of Model 1 by Kim et al. (2023) (Model 4). Their

evaluation indicated that Model 4 outperformed Model 1 in terms of event detectability for the Hakone data. To evaluate the applicability of Model 4 for the Kirishima data, we used Model 4 to estimate the seismic catalog for the period 2016–2019 using the aforementioned workflow. We detected around twice as many earthquakes as in the seismic catalog obtained using Model 1 for the same period (Additional file 1: Fig. S12). However, the seismic catalog created with Model 4 also included numerous false detections. For example, many earthquakes were detected immediately after the occurrence of 2016 Kumamoto earthquake (Additional file 1: Fig. S12). Upon visually inspecting the automatically picked P - and S -wave onsets in the waveforms of these events, we determined that the false detections were a result of Model 4 identifying the P - and S -wave trains from the aftershocks of the Kumamoto earthquake as different earthquakes. This result indicates that Model 1 is versatile enough to reflect the general characteristics of earthquake waveforms in various volcanic regions, while Model 4 is more specifically targeted to the Hakone data.

In contrast, a comparison of the normalized cumulative curves between the JMA and ML catalogs prior to the 2011 eruption (Additional file 1: Fig. S13) revealed no notable detection enhancement for the ML catalog compared to the JMA catalog. We interpret this lack of enhancement to be due to the limited number of available stations during this period. However, the increases in seismicity before the 2017 and 2018 eruptions at Shinmoedake and the 2019 phreatic eruption at Iwo-Yama were considerably better revealed by the ML catalog than by the JMA catalog.

We evaluated the time difference between manually and automatically picked phases for ~ 400 events in the ML catalog from June 2008 to February 2011 (Fig. 5). Additional file 1: Figure S14 provides examples of waveform records with manually and automatically picked arrival times for earthquakes occurring beneath Shinmoedake. No significant difference in travel time for P -wave onsets was evident between manually and automatically picked data. Similarly, insignificant differences for P -wave onsets were found for the Hakone volcano (Kim et al. 2023). In contrast, several S -wave onsets showed large differences in arrival times between manually and automatically picked data compared with P -wave onsets. We also estimated precision, recall, and F1 score (e.g., Zhu and Beroza 2019) for P - and S -wave phase picking. Arrival time differences of less than 0.1 s were counted as true positives following the definition by Zhu and Beroza (2019). Precision, recall, and F1 scores were 0.994, 0.994, and 0.994 for P -waves and 0.854, 0.747, and 0.797 for S -waves. These results reflect the difficulty in picking the arrival time of the S -wave due

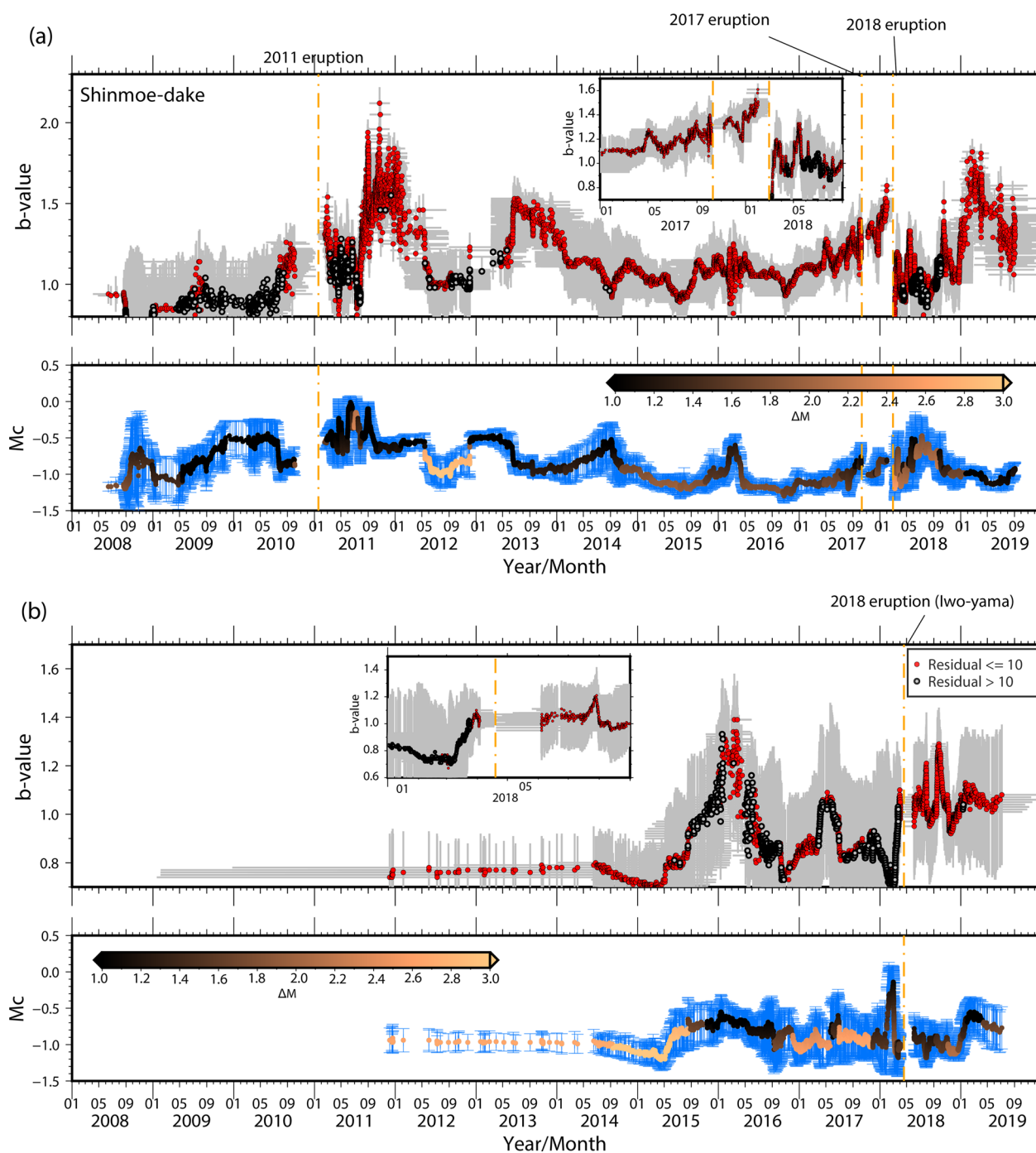


Fig. 4 Temporal changes in b values and M_c as estimated using the goodness-of-fit method (Wiemer and Wyss 2002) for **a** Shinmoedake and **b** Iwo-Yama. The horizontal and vertical lines at each point show the time window for selecting the earthquakes and the error bar of the datum (b value in the top panel, M_c in the bottom panel) as estimated using the bootstrap resampling method. In the top panel, red circles represent reliable b value estimations with residuals for the theoretical Gutenberg–Richter law distribution $\leq 10\%$. Color in the bottom panel shows the magnitude bandwidth, which is equal to the largest magnitude minus the M_c in each time window. Inset diagrams in the top panel in **a** and **b** show magnified plots around the 2017 and 2018 eruptions at Shinmoedake and the 2018 eruption at Iwo-Yama, respectively

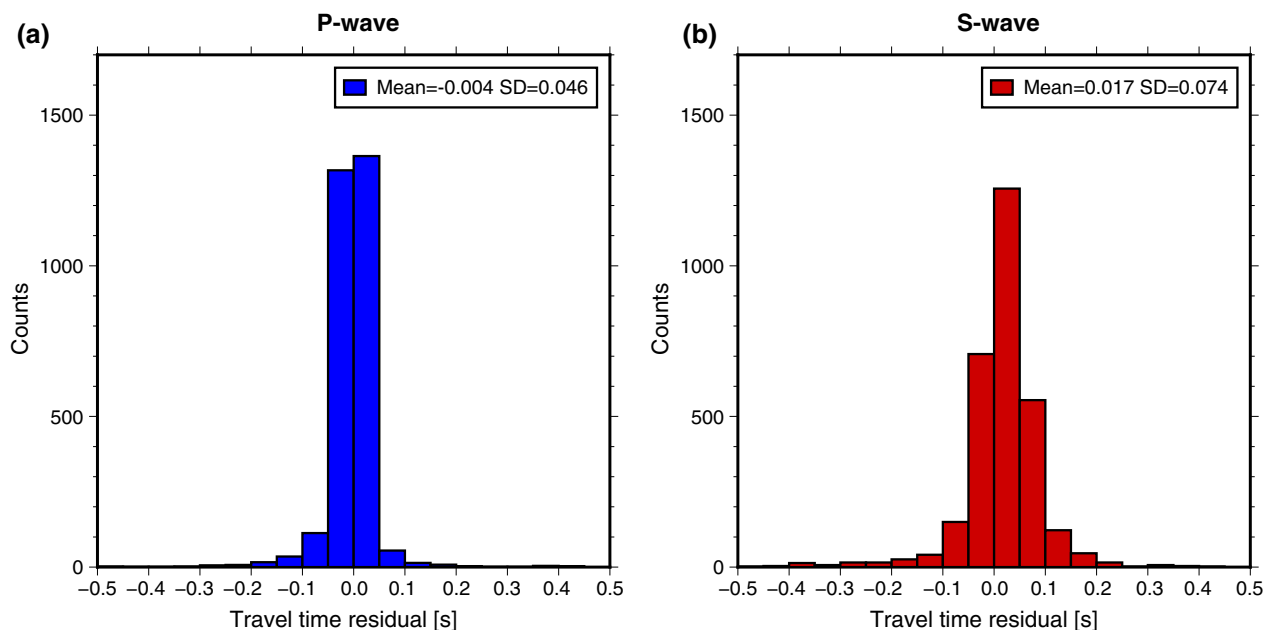


Fig. 5 Frequency distribution of the time difference between the manually and automatically picked phases. Values in the upper right corner indicate the mean and standard deviation. **a** P-wave and **b** S-wave

to the contaminating effect of wave scattering caused by structural heterogeneity. However, these uncertainties in phase picking are expected to be reduced by estimating travel time differences using cross-correlation analysis during DD relocation.

We compared the final ML catalog with that derived from the original trained model developed by Zhu and Beroza (2019) from 2017 to 2019 to evaluate the performance of the trained model based on volcanic earthquakes (Kim et al. 2023). Although the main characteristics of hypocenter distributions did not differ considerably between the two catalogs (Additional file 1: Fig. S15), we detected ~15% more earthquakes using the learning model derived from volcanic earthquakes in the Hakone region (Model 1) than using the original model trained on tectonic earthquakes in California. Additional file 1: Figures S16 and 6 show the magnitude–frequency distribution and hypocenter distribution, respectively, of the newly detected events by Model 1. Many earthquakes of small magnitude, particularly those occurring at shallow depths beneath Shinmoedake and Iwo-Yama, were successfully detected using Model 1. However, we must note that several events were detected only by the original trained model by Zhu and Beroza (2019) and not by the model trained on volcanic earthquakes. Although both trained models missed several earthquakes, our model trained on volcanic earthquakes showed better performance than the original model in detecting small earthquakes. The accuracy of automatic phase picking

may be further improved by modifying the trained model through transfer learning (e.g., Lapins et al. 2021) or fine-tuning using the manual picking data at the Kirishima volcano. This issue will be addressed in future work.

The highly resolved seismic catalog provides important information that may correspond to precursory or unrest signals prior to eruptions. We detected the activation of volcanic earthquakes before the eruptions at Shinmoedake and Iwo-Yama (Fig. 2). We clearly detected gradual increases in seismicity (Fig. 2) and b value (Fig. 4 and Additional file 1: Fig. S17) leading up to the 2017 and 2018 eruptions at Shinmoedake which are less pronounced in the JMA catalog (Additional file 1: Figs. S7 and S13) and other routine seismic catalogs (Yamada et al. 2019). The 2017 and 2018 eruptions at Shinmoedake occurred when the b values were close to 1.5 (Fig. 4a). The high b values observed during fluid-induced seismicity are interpreted to reflect a low shear stress level on fault planes (Mukuhira et al. 2021). The activation of volcanic earthquakes with increasing b values is caused by an elevation in magmatic fluid pressure (Nanjo et al. 2018). The high b values with increasing seismic activity before an eruption (Figs. 2 and 4) may reflect unstable conditions in and around a volcanic conduit due to the increase in fluid pressure accompanied by the supply of magma. Ichihara et al. (2023) showed a gradual increase in the seismic background level (SBL) at stations near Shinmoedake starting in early 2017. They interpreted the increase in SBL during this period as reflecting interactions between

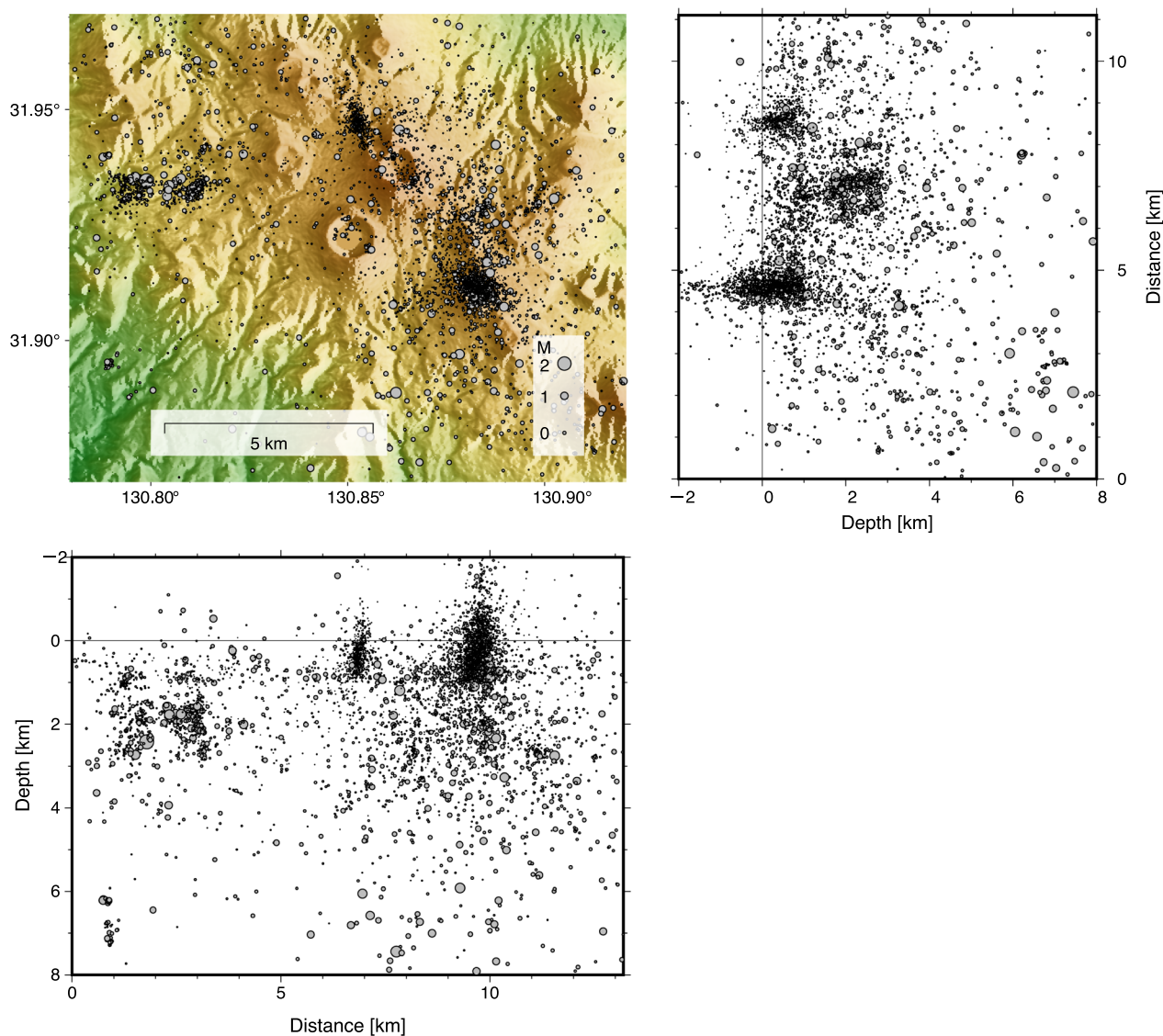


Fig. 6 Hypocenter distribution of earthquakes detected only by the trained model of Kim et al. (2023) during 2017–2019

the shallow water table and the slowly migrating magmatic fluid prior to the 2017 Shinmoedake eruption. The timing of seismic activation and b value increase in 2017 is mostly consistent with that of the SBL elevation. These observations likely reflect changes in the shallow hydrothermal system beneath Shinmoedake due to the supply of magmatic fluid during the precursory period. On the other hand, sufficient earthquake data were not obtained before the 2011 eruption at Shinmoedake. Moreover, during 2009–2010, the estimation of b values is less reliable due to the narrow bandwidth of magnitude (Fig. 4). Therefore, the detailed temporal sequence of b values preceding the 2011 eruption could not be discussed in this study. We also observed an abrupt increase in b

values prior to the 2018 eruption at Iwo-Yama (Fig. 4b), although this increase is difficult to quantify because of the large uncertainty in the b value estimates. The b value gradually increased toward the end of 2015 and again in the middle of 2017 (Fig. 4b). Aizawa et al. (2022) documented several episodes of rapid tilt changes accompanied by volcanic tremors and electric-field changes near the vent of the phreatic eruption during late 2015, August 2014, and mid-2017, as well as before the 2018 phreatic eruption. They interpreted these episodes as repeated intrusions of hydrothermal fluid. Fumarolic activity at Iwo-Yama resumed in December 2015 (Tajima et al. 2020). Shallow seismic activity in this region occurred beneath the low-resistivity layer, which is interpreted

as the low-permeability cap structure developed in the hydrothermal system (Tsukamoto et al. 2018). These results reveal that the b value increase observed at Iwo-Yama reflects an increase in the pore-fluid pressure beneath the cap structure due to the intrusion of hydrothermal fluid.

Our seismic catalog also reveals the highly resolved hypocenter distribution of volcanic earthquakes beneath the crater at Shinmoedake (Fig. 3a) compared with the JMA catalog. The cylindrical hypocenter distribution vertically extending with a radius of ~ 500 m within the depth range of 1.0 to -0.5 km includes the source locations of volcanic tremors during the magmatic eruptions in 2011, 2017, and 2018 (Ichihara and Matsumoto 2017; Ichihara et al. 2023). They interpreted that a continuous tremor signal was generated during magmatic fluid movement. The hypocenter distribution of volcanic earthquakes (Fig. 3a) may reflect the structure of the magma pathway in the shallow part of the volcanic conduit.

We also detected the activation of low-frequency earthquakes before 2011, 2017, and 2018 Shinmoedake eruptions (Fig. 2d). The increase in the ratio of low-frequency earthquakes to volcano-tectonic earthquakes before eruptions may reflect the interaction between magmatic and shallow hydrothermal fluids (e.g., McNutt 1996). The activation of low-frequency earthquakes at the deeper part of the volcano (deeper than 10 km) and crustal expansions due to an inflation of pressure source at a depth of 8 km were detected ~ 1 year before the 2011 eruptions, suggesting the supply of magma into the volcanic root (Kurihara et al. 2019; Nakao et al. 2013). The rapid increase in the ratio of low-frequency earthquakes since April 2010 suggests the supply of new magmatic fluid into the shallow part beneath the volcanic conduit. The number of low-frequency earthquakes slightly increased from 2014 to 2015 (Fig. 2b). Although no eruptions occurred during this period, an expansion of the GPS baseline length was observed (Kurihara et al. 2019), indicating the initiation of a magmatic fluid supply. The cluster of low-frequency earthquakes at a depth of 3 km beneath Karakuni-dake (Fig. 1) corresponds to the upper extension of the subvertical conductive body, which is interpreted as a magma pathway (Aizawa et al. 2014). The low-frequency earthquakes in this cluster may have been triggered by the migration of magmatic fluid at this depth.

Using the ML architecture developed by Zhu and Beroza (2019) and a trained model from the seismic catalog of the Hakone volcano (Kim et al. 2023), we obtained a high-quality seismic catalog of volcanic earthquakes at the Kirishima volcano from 2008 to 2019. We produced a seismic catalog with higher detectability than the conventional seismic catalog based on manual phase picking

and estimated the highly resolved hypocenter distribution through relative hypocenter relocation using wave cross-correlation analysis. From the seismic catalog, the activation of volcanic earthquakes and increment of b values were detected preceding the magmatic and phreatic eruptions at the Kirishima volcano. This improved detectability enables the evaluation of eruption risks through statistical analysis based on b values and the temporal sequence of low-frequency earthquake activity, as well as the spatial–temporal sequence of volcanic earthquakes. Using a standard Linux machine, the computation time required to obtain the initial hypocenters for a 1-h waveform record of 30 stations is only a few minutes. Therefore, this system contributes to the improvement of our ability to perform eruption forecasting.

Abbreviations

| | |
|------|---|
| BVS | b Value stability |
| DD | Double difference |
| ERI | Earthquake Research Institute, the University of Tokyo |
| FI | Frequency index |
| GFT | Goodness of fit |
| JMA | Japan Meteorological Agency |
| LF | Low frequency |
| LTA | Long-term average |
| ML | Machine learning |
| NIED | National Research Institute for Earth Science and Disaster Resilience |
| SBL | Seismic background level |
| SN | Signal to noise |
| STA | Short-term average |

Supplementary Information

The online version contains supplementary material available at <https://doi.org/10.1186/s40623-023-01939-9>.

Additional file 1: Figure S1. Estimated 1D velocity model and station corrections. (a) 1D velocity model for P- and S-waves; the Vp/Vs structure is shown on the right. The dotted lines represent the initial velocity, and the solid lines represent the velocity model modified by the JHD method. (b) Station (travel time) corrections for the P-waves (left) and S-waves (right). Circles show positive travel time residuals (i.e., an observed travel time is later than a theoretical one), while crosses show negative travel time residuals. **Figure S2.** Comparison of frequency distribution of the travel time residuals between the initial hypocenters ((a) and (b)) and the relocated hypocenter ((c) and (d)) by applying the modified 1D velocity model and station corrections. **Figure S3.** Temporal changes in b -values and M_c as estimated using the maximum curvature method. The horizontal and vertical lines at each point show the time window for selecting the earthquakes and the error bar of the b -value (top panel) or M_c (bottom panel) as estimated using the bootstrap resampling method. The color spectrum in the bottom figure shows the delta M value or magnitude bandwidth equal to the largest magnitude minus M_c in each time window. Please note that the seismic catalog is not split before and after the eruption occurrence time. **Figure S4.** Temporal changes in b -values and M_c values as estimated using the goodness-of-fit test. **Figure S5.** Temporal changes in b -values and M_c values estimated using the b -value stability method. **Figure S6.** Hypocenter distribution of the earthquake beneath the Kirishima volcano in the JMA catalog. The top panel shows the epicentral distribution, and the top-right and bottom panels indicate the depth distribution along the N–S and E–W sections, respectively. The depth of 0 km corresponds to the sea level. **Figure S7.** Depth–time distribution and cumulative number of earthquakes in the JMA catalog. The blue lines indicate the cumulative curve containing volcano tectonic and low-frequency

earthquakes. The black circles indicate the depth–time plot of the earthquakes. The dotted vertical yellow lines show the occurrence times of the main events: the 2011 Shinmoedake eruption, the 2016 Kumamoto earthquake, the 2017 and 2018 Shinmoedake eruptions, and the 2018 Iwo-yama phreatic eruption. (a) Whole region, (b) Shinmoedake, and (c) Iwo-Yama. The regions of Shinmoedake and Iwo-Yama correspond to the maps shown in Figures 3a and 3b, respectively. **Figure S8.** Comparison of magnitude–frequency distribution between two seismic catalogs: (a) ML and (b) JMA. Squares represent cumulative magnitude–frequency distribution; triangles represent the number of events in each magnitude bin; blue inverted triangles represent M_c ; and red lines represent linear regressions for both catalogs. **Figure S9.** Comparison of the amplitude spectra of the seismograms of A-type (blue line) and B-type (red line) earthquakes based on the JMA catalog. The light blue and red lines show several examples of spectrograms of B- and A-type earthquakes, respectively. The dark blue and red lines show the stacked spectrograms. (a) EV. KVO and (b) EV. EBS stations. **Figure S10.** (a) and (b) shows frequency distribution of FI values obtained at (a) EV. KVO and (b) EV. EBS stations. We estimated the median of FI values at each station and subtracted it from the estimated FI values. (c) Frequency distribution of the standard deviation for the final FI values after applying the station correction. **Figure S11.** Relationship between FI and magnitude: (a) JMA catalog and (b) ML catalog. (c) and (d) show examples of waveform records in the EW component at EV. KAR station. (c) and (d) correspond to the waveforms of low-frequency and volcano-tectonic earthquakes in ML catalog classified based on the FI value, respectively. The text at the top of (c) and (d) indicates the origin time, latitude, longitude, depth, magnitude, and FI value of the earthquake. **Figure S12.** Hypocenter distribution, depth–time distribution, and cumulative number of earthquakes during 2016–2019 detected using Model 4 by Kim et al. (2023). Hypocenters were relocated using the DD method. **Figure S13.** Comparison of cumulative numbers of earthquake between JMA (blue line) and ML (red line) catalogs. (a) Whole region, (b) Shinmoedake, and (c) Iwo-Yama. The regions of Shinmoedake and Iwo-Yama correspond to the maps shown in Figures 3a and 3b, respectively. **Figure S14.** Examples of waveform records of vertical motion, showing manually picked (solid line) and automatically (broken line) picked arrival times. The red and blue lines show the onset times of the *P* and *S* waves, respectively. The text in the upper portion of each panel indicates the origin time and magnitude. **Figure S15.** Comparison of the initial hypocenters before the DD relocation and their temporal seismicity sequence during 2017–2019: (a) learning model derived from volcanic earthquakes (Kim et al., 2023) and (b) original learning model by Zhu and Beroza (2018). The dotted vertical yellow lines in each bottom panel show the occurrence time of the main events, as shown in Figure 54. **Figure S16.** Histograms showing the frequency distribution of magnitude for earthquakes detected by the model trained on the volcanic earthquake catalog (Kim et al. 2023) from 2017 to 2019. (Left) Blue bins constitute a histogram for all events; red bins constitute a histogram for only those events detected by the trained model of Kim et al. (2023) (Model 1). (Right) Red bins constitute a histogram for only those events detected by the trained model of Zhu and Beroza (2019). **Figure S17.** Example of Magnitude–frequency distribution of earthquakes beneath Shinmoedake for two periods: (left) March 1, 2016–July 24, 2016 (right) January 2, 2018–February 27, 2018. Each panel contains 300 events, which is the same number of events used to estimate the temporal distribution of *b*-value in Figure 4 of the main text. Red line represent linear regressions.

Acknowledgements

We used seismic waveform data obtained by the Japan Meteorological Agency (JMA), the National Research Institute for Earth Science and Disaster Prevention, Kyushu University, and the Earthquake Research Institute of the University of Tokyo. JMA provided us with the hypocenter catalog of volcanic earthquakes. We also thank the three anonymous reviewers and the editor, Dr. Kostas Konstantinou, for their insightful comments. Dr. Jun Oikawa provided the manual picking data at the Kirishima volcano.

Author contributions

YY analyzed the data and wrote the manuscript. AK supported data processing and assisted with interpretation of the results. TO carried out seismic observations. All authors have read and approved the final manuscript.

Funding

This study was supported by JSPS KAKENHI Grant No. 22K03752 and the Next Generation Volcano Research and Human Resource Development Project of the Ministry of Education, Culture, Sports, and Science and Technology of Japan.

Availability of data and materials

The waveform data are obtainable from the website of NIED Hi-net (National Research Institute for Earth Science and Disaster Resilience 2019). The hypocenter catalog obtained in this study can be downloaded from the data repository (Yukutake 2023). Most of the figures in this study were created using Generic Mapping Tools software (Wessel et al. 2019). The *b* values were calculated using the ZMAP program (Wiemer 2001). The code of hypomh_ps is available from the author upon reasonable request.

Declarations

Ethics approval and consent to participate

Not applicable.

Consent for publication

Not applicable.

Competing interests

The authors declare that they have no competing interests.

Author details

¹Earthquake Research Institute, The University of Tokyo, 1-1-1 Yayoi Bunkyo-ku, Tokyo, Japan. ²Yokohama City University, 22-2 Seto, Kanazawa-ku, Yokohama, Kanagawa 236-0027, Japan.

Received: 4 April 2023 Accepted: 21 November 2023

Published online: 07 December 2023

References

- Aizawa K et al (2014) Three-dimensional resistivity structure and magma plumbing system of the Kirishima Volcanoes as inferred from broadband magnetotelluric data. *J Geophys Res* 119:198–215. <https://doi.org/10.1002/2013JB010682>
- Aizawa K, Muramatsu D, Matsushima T, Koyama T, Uyeshima M, Nakao S (2022) Phreatic volcanic eruption preceded by observable shallow groundwater flow at Iwo-Yama, Kirishima Volcanic Complex, Japan. *Commun Earth Environ* 3:187. <https://doi.org/10.1038/s43247-022-00515-5>
- Aki K (1965) Maximum likelihood estimate of *b* in the formula $\log N = a - bM$ and its confidence limits. *Bull Earthq Res Inst Univ Tokyo* 43:237–239
- Asano K, Iwata T (2016) Source rupture processes of the foreshock and mainshock in the 2016 Kumamoto earthquake sequence estimated from the kinematic waveform inversion of strong motion data. *Earth Planets Space* 68:147. <https://doi.org/10.1186/s40623-016-0519-9>
- Cao A, Gao SS (2002) Temporal variation of seismic *b*-values beneath north-eastern Japan island arc. *Geophys Res Lett* 29:48–41–48–43. <https://doi.org/10.1029/2001GL013775>
- Fukuoka District Meteorological Observatory Kagoshima Local Meteorological Observatory (2013) The 2011 Eruptive Activities of Shinmoedake Volcano, Kirishimayama, Kyushu, Japan. *J Seismol Volcanol Relat Eng* 77:65–96
- Gal M, Lotter E, Olivier G, Green M, Meyer S, Dales P, Reading AM (2021) CCLoc—an improved interferometric seismic event location algorithm applied to induced seismicity. *Seismol Res Lett* 92:3492–3503. <https://doi.org/10.1785/0220210068>

- Gulia L, Tormann T, Wiemer S, Herrmann M, Seif S (2016) Short-term probabilistic earthquake risk assessment considering time-dependent b values. *Geophys Res Lett* 43:1100–1108. <https://doi.org/10.1002/2015GL066686>
- Hayashi Y, Morita Y (2003) An image of a magma intrusion process inferred from precise hypocentral migrations of the earthquake swarm east of the Izu Peninsula. *Geophys J Int* 153:159–174. <https://doi.org/10.1046/j.1365-246X.2003.01892.x>
- Helena B, Michael EW (2010) Seismic precursors to volcanic explosions during the 2006 eruption of Augustine Volcano: Chapter 2 in The 2006 eruption of Augustine Volcano, Alaska. Professional Paper. p 41–57. <https://doi.org/10.3133/pp17692>
- Hirata N, Matsu'ura M (1987) Maximum-likelihood estimation of hypocenter with origin time eliminated using nonlinear inversion technique. *Phys Earth Planet Inter* 47:50–61. [https://doi.org/10.1016/0031-9201\(87\)90066-5](https://doi.org/10.1016/0031-9201(87)90066-5)
- Ichihara M, Matsumoto S (2017) Relative source locations of continuous tremor before and after the subplinian events at Shinmoe-dake, in 2011. *Geophys Res Lett* 44:10871–810877. <https://doi.org/10.1002/2017gl075293>
- Ichihara M, Ohminato T, Konstantinou KI, Yamakawa K, Watanabe A, Takeo M (2023) Seismic background level (SBL) growth can reveal slowly developing long-term eruption precursors. *Sci Rep* 13:5954. <https://doi.org/10.1038/s41598-023-32875-z>
- Imura T, Kobayashi T (2001) Geological Map OF Kirishima Volcano vol 11. Geological map of volcanos, vol 1. Geological Survey of Japan
- Imura R, Kobayashi T (1991) Eruptions of Shinmoedake Volcano, Kirishima Volcano Group, in the last 300 years. *Bull Volc Soc Jpn* 36:135–148. https://doi.org/10.18940/kazan.36.2_135
- Kato A, Terakawa T, Yamanaka Y, Maeda Y, Horikawa S, Matsuhiro K, Okuda T (2015) Preparatory and precursory processes leading up to the 2014 phreatic eruption of Mount Ontake, Japan. *Earth Planets Space* 67:1–11. <https://doi.org/10.1186/s40623-015-0288-x>
- Kawanishi R, Iio Y, Yukutake Y, Shibutani T, Katao H (2009) Local stress concentration in the seismic belt along the Japan Sea coast inferred from precise focal mechanisms: Implications for the stress accumulation process on intraplate earthquake faults. *J Geophys Res*. <https://doi.org/10.1029/2008jb005765>
- Kim A, Nakamura Y, Yukutake Y, Uematsu H, Abe Y (2023) Development of a high-performance seismic phase picker using deep learning in the Hakone volcanic area. *Earth Planets Space* 75:85. <https://doi.org/10.1186/s40623-023-01840-5>
- Kissling E, Ellsworth WL, Eberhart-Phillips D, Kradolfer U (1994) Initial reference models in local earthquake tomography. *J Geophys Res* 99:19635–19646. <https://doi.org/10.1029/93JB03138>
- Konstantinou KI (2022) Multiyear temporal variation of b-values at Alaskan volcanoes: the synergetic influence of stress and material heterogeneity. *J Volcanol Geotherm Res* 427:107572. <https://doi.org/10.1016/j.jvolgeores.2022.107572>
- Kurihara R, Obara K, Takeo A, Tanaka Y (2019) Deep low-frequency earthquakes associated with the eruptions of Shinmoe-dake in Kirishimavolcanoes. *J Geophys Res* 124:13079–13095. <https://doi.org/10.1029/2019jb018032>
- Lapins S, Goitom B, Kendall J-M, Werner MJ, Cashman KV, Hammond JOS (2021) A little data goes a long way: automating seismic phase arrival picking at nabro volcano with transfer learning. *J Geophys Res* 126:e2021JB021910. <https://doi.org/10.1029/2021JB021910>
- Maeno F et al (2023) Eruption style transition during the 2017–2018 eruptive activity at the Shinmoedake volcano, Kirishima, Japan: surface phenomena and eruptive products. *Earth Planets Space* 75:76. <https://doi.org/10.1186/s40623-023-01834-3>
- Matoza RS, Shearer PM, Okubo PG (2014) High-precision relocation of long-period events beneath the summit region of Kilauea Volcano, Hawai'i, from 1986 to 2009. *Geophys Res Lett* 41:3413–3421. <https://doi.org/10.1002/2014GL059819>
- McNutt SR (1996) Seismic monitoring and eruption forecasting of volcanoes: a review of the state-of-the-art and case histories. In: Scarpa R, Tilling RI (eds) *Monitoring and mitigation of volcano hazards*. Springer, Berlin Heidelberg, pp 99–146. https://doi.org/10.1007/978-3-642-80087-0_3
- Mikada H (1996) A seismic reflection analysis on refraction data from the 1994 Kirishima explosion experiment. *Bull Volc Soc Japan* 41:159–170. https://doi.org/10.18940/kazan.41.4_159
- Minakami T (1974) Chapter 1-Seismology of volcanoes in Japan. In: Civetta L, Gasparini P, Luongo G, Rapolla A (eds) *Developments in solid earth geophysics*, vol 6. Elsevier, Amsterdam, pp 1–27. <https://doi.org/10.1016/B978-0-444-41141-9.50007-3>
- Mousavi SM, Ellsworth WL, Zhu W, Chuang LY, Beroza GC (2020) Earthquake transformer—an attentive deep-learning model for simultaneous earthquake detection and phase picking. *Nat Commun* 11:3952. <https://doi.org/10.1038/s41467-020-17591-w>
- Mukuhira Y, Fehler MC, Ito T, Asanuma H, Häring MO (2021) Injection-induced seismicity size distribution dependent on shear stress. *Geophys Res Lett* 48:e2020GL090934. <https://doi.org/10.1029/2020GL090934>
- Münchmeyer J et al (2022) Which picker fits my data? A quantitative evaluation of deep learning based seismic pickers. *J Geophys Res* 127:e2021JB023499. <https://doi.org/10.1029/2021JB023499>
- Nakada S, Nagai M, Kaneko T, Suzuki Y, Maeno F (2013) The outline of the 2011 eruption at Shinmoe-dake (Kirishima), Japan. *Earth Planets Space* 65:475–488. <https://doi.org/10.5047/eps.2013.03.016>
- Nakano M, Sugiyama D, Hori T, Kuwatani T, Tsuboi S (2019) Discrimination of seismic signals from earthquakes and tectonic tremor by applying a convolutional neural network to running spectral images. *Seismol Res Lett* 90:530–538. <https://doi.org/10.1785/0220180279>
- Nakao S et al (2013) Volume change of the magma reservoir relating to the 2011 Kirishima Shinmoe-dake eruption—Charging, discharging and recharging process inferred from GPS measurements. *Earth Planets Space* 65:3. <https://doi.org/10.5047/eps.2013.05.017>
- Nanjo KZ, Miyaoka K, Tamaribuchi K, Kobayashi A, Yoshida A (2018) Related spatio-temporal changes in hypocenters and the b value in the 2017 Kagoshima Bay swarm activity indicating a rise of hot fluids. *Tectonophysics* 749:35–45. <https://doi.org/10.1016/j.tecto.2018.10.023>
- National Research Institute for Earth Science and Disaster Resilience (2019) NIED Hi-net, National Research Institute for Earth Science and Disaster Resilience. <https://doi.org/10.17598/NIED.0003>
- Peng Z, Zhao P (2009) Migration of early aftershocks following the 2004 Parkfield earthquake. *Nat Geosci* 2:877–881. <https://doi.org/10.1038/ngeo697>
- Perol T, Gharbi M, Denolle M (2018) Convolutional neural network for earthquake detection and location. *Sci Adv* 4:e1700578. <https://doi.org/10.1126/sciadv.1700578>
- Poiata N, Satriano C, Vilotte J-P, Bernard P, Obara K (2016) Multiband array detection and location of seismic sources recorded by dense seismic networks. *Geophys J Int* 205:1548–1573. <https://doi.org/10.1093/gji/ggw071>
- Roberts NS, Bell AF, Main IG (2015) Are volcanic seismic b-values high, and if so when? *J Volcanol Geotherm Res* 308:127–141. <https://doi.org/10.1016/j.jvolgeores.2015.10.021>
- Ross ZE, Cochran ES, Trugman DT, Smith JD (2020) 3D fault architecture controls the dynamism of earthquake swarms. *Science* 368:1357–1361. <https://doi.org/10.1126/science.abb0779>
- Shelly DR, Beroza GC, Ide S (2007) Non-volcanic tremor and low-frequency earthquake swarms. *Nature* 446:305–307. <https://doi.org/10.1038/nature05666>
- Shelly DR, Hill DP, Massin F (2013) A fluid-driven earthquake swarm on the margin of the Yellowstone caldera. *J Geophys Res*. <https://doi.org/10.1002/jgrb.50362>
- Sugiyama D, Tsuboi S, Yukutake Y (2021) Application of deep learning-based neural networks using theoretical seismograms as training data for locating earthquakes in the Hakone volcanic region, Japan. *Earth Planets Space* 73:135. <https://doi.org/10.1186/s40623-021-01461-w>
- Tajima Y et al (2020) Shallow Magmatic hydrothermal eruption in April 2018 on Ebinokogen Ioyama volcano in Kirishima volcano group, Kyushu, Japan. *Geosciences* 10:183
- Toda S, Stein RS, Sagiya T (2002) Evidence from the AD 2000 Izu islands earthquake swarm that stressing rate governs seismicity. *Nature* 419:58–61
- Tsukamoto K et al (2018) Three-Dimensional resistivity structure of Iwo-Yama volcano, kirishima volcanic complex, Japan: relationship to shallow seismicity, surface uplift, and a small phreatic eruption. *Geophys Res Lett* 45:12821–812828. <https://doi.org/10.1029/2018GL080202>
- Waldhauser F, Ellsworth WL (2000) A double-difference earthquake location algorithm: method and application to the northern Hayward fault, California. *Bull Seismol Soc Am* 90:1353–1368. <https://doi.org/10.1785/0120000006>

- Watanabe H (1971) Determination of earthquake magnitude at regional distance in and near Japan. *Zisin* 24:189–200. https://doi.org/10.4294/zisin1948.24.3_189
- Wessel P, Luis JF, Uieda L, Scharroo R, Wobbe F, Smith WHF, Tian D (2019) The generic mapping tools version 6. *Geochem Geophys Geosyst* 20:5556–5564. <https://doi.org/10.1029/2019GC008515>
- Wiemer S (2001) A software package to analyze seismicity: ZMAP. *Seismol Res Lett* 72:373–382. <https://doi.org/10.1785/gssrl.72.3.373>
- Wiemer S, Wyss M (2000) Minimum magnitude of completeness in earthquake catalogs: examples from Alaska, the western United States, and Japan. *Bull Seismol Soc Am* 90:859–869. <https://doi.org/10.1785/0119990114>
- Wiemer S (2002) Mapping spatial variability of the frequency-magnitude distribution of earthquakes. *Adv Geophys* 45:259–302
- Wilding JD, Zhu W, Ross ZE, Jackson JM (2022) The magmatic web beneath Hawai'i. *Science* 379:462–468. <https://doi.org/10.1126/science.ade5755>
- Yamada T, Ueda H, Mori T, Tanada T (2019) Tracing volcanic activity chronology from a multiparameter dataset at Shinmoedake Volcano (Kirishima), Japan. *J Disaster Res* 14:687–700. <https://doi.org/10.20965/jdr.2019.p0687>
- Yukutake Y (2023) Earthquake catalog of volcanic earthquake beneath the Kirishima volcano, southwest Japan. *figshare*. <https://doi.org/10.6084/m9.figshare.24557026>
- Zhang M, Ellsworth WL, Beroza GC (2019) Rapid earthquake association and location. *Seismol Res Lett* 90:2276–2284. <https://doi.org/10.1785/0220190052>
- Zhu W, Beroza GC (2019) PhaseNet: a deep-neural-network-based seismic arrival-time picking method. *Geophys J Int* 216:261–273. <https://doi.org/10.1093/gji/ggy423>

Publisher's Note

Springer Nature remains neutral with regard to jurisdictional claims in published maps and institutional affiliations.

Submit your manuscript to a SpringerOpen® journal and benefit from:

- ▶ Convenient online submission
- ▶ Rigorous peer review
- ▶ Open access: articles freely available online
- ▶ High visibility within the field
- ▶ Retaining the copyright to your article

Submit your next manuscript at ▶ [springeropen.com](https://www.springeropen.com)
